



**Please cite the Published Version**

Sharp, Jonathan, Ciotti, Anna, Andrews, Hayley, Udayasurian, Shaktiswaran R, García-Melchor, Max  and Li, Tengfei  (2024) Sustainable electrosynthesis of cyclohexanone oxime through nitrate reduction on a Zn-Cu alloy catalyst. ACS Catalysis, 14 (5). pp. 3287-3297. ISSN 2155-5435

**DOI:** <https://doi.org/10.1021/acscatal.3c05388>

**Publisher:** American Chemical Society (ACS)

**Version:** Published Version

**Downloaded from:** <https://e-space.mmu.ac.uk/634603/>

**Usage rights:**  [Creative Commons: Attribution 4.0](https://creativecommons.org/licenses/by/4.0/)

**Additional Information:** This is an open access article which first appeared in ACS Catalysis

**Enquiries:**

If you have questions about this document, contact [openresearch@mmu.ac.uk](mailto:openresearch@mmu.ac.uk). Please include the URL of the record in e-space. If you believe that your, or a third party's rights have been compromised through this document please see our Take Down policy (available from <https://www.mmu.ac.uk/library/using-the-library/policies-and-guidelines>)

# Sustainable Electrosynthesis of Cyclohexanone Oxime through Nitrate Reduction on a Zn–Cu Alloy Catalyst

Jonathan Sharp,<sup>§</sup> Anna Ciotti,<sup>§</sup> Hayley Andrews, Shaktiswaran R. Udayasurian, Max García-Melchor,<sup>\*</sup> and Tengfei Li<sup>\*</sup>



Cite This: *ACS Catal.* 2024, 14, 3287–3297



Read Online

ACCESS |

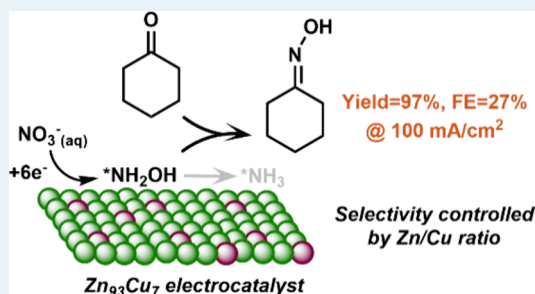
Metrics & More

Article Recommendations

Supporting Information

**ABSTRACT:** Cyclohexanone oxime is an important precursor for Nylon-6 and is typically synthesized via the nucleophilic addition–elimination of hydroxylamine with cyclohexanone. Current technologies for hydroxylamine production are, however, not environment-friendly due to the requirement of harsh reaction conditions. Here, we report an electrochemical method for the one-pot synthesis of cyclohexanone oxime under ambient conditions with aqueous nitrate as the nitrogen source. A series of Zn–Cu alloy catalysts are developed to drive the electrochemical reduction of nitrate, where the hydroxylamine intermediate formed in the electroreduction process can undergo a chemical reaction with the cyclohexanone present in the electrolyte to produce the corresponding oxime. The best performance is achieved on a  $Zn_{93}Cu_7$  electrocatalyst with a 97% yield and a 27% Faradaic efficiency for cyclohexanone oxime at 100 mA/cm<sup>2</sup>. By analyzing the catalytic activities/selectivities of the different Zn–Cu alloys and conducting in-depth mechanistic studies via *in situ* Raman spectroscopy and theoretical calculations, we demonstrate that the adsorption of nitrogen species plays a central role in catalytic performance. Overall, this work provides an attractive strategy to build the C–N bond in oxime and drive organic synthesis through electrochemical nitrate reduction, while highlighting the importance of controlling surface adsorption for product selectivity in electrosynthesis.

**KEYWORDS:** nitrate electroreduction, cyclohexanone oxime, C–N bond formation, electrosynthesis, Zn–Cu alloy catalyst, DFT calculations, reaction mechanisms



## INTRODUCTION

Cyclohexanone oxime is an important feedstock in the nitrogen industry as it can undergo Beckmann rearrangement to make caprolactam, the monomeric unit of Nylon-6. With the annual global market of Nylon-6 anticipated to be as high as 8.9 million tons by 2024,<sup>1</sup> the production capacity of cyclohexanone oxime should also be expanded accordingly. To date, the majority of cyclohexanone oxime is produced by the nucleophilic addition–elimination reaction between cyclohexanone and hydroxylamine ( $NH_2OH$ ),<sup>2</sup> which is typically generated via hydrogenation of  $NO_x$  on palladium catalysts<sup>3</sup> or oxidation of ammonia ( $NH_3$ ) by  $O_2/H_2O_2$  (Figure 1a).<sup>4–6</sup> However, these chemical processes generally require harsh reaction conditions (e.g., high temperatures and/or pressures, strong acidic/alkaline solutions) and therefore are challenged by a series of environmental and safety concerns. More specifically, the hydrogenation route is limited by the requirements of pressurized  $H_2$  gas, strong acidic conditions and precious metal catalysts. Moreover, transportation and storage of concentrated  $NH_2OH$  also faces challenges, including the risk of explosion.<sup>7</sup> On the other hand,  $NH_3$  oxidation utilizes  $NH_2OH$  generated *in situ* as needed.<sup>4</sup> Yet, this synthetic route still demands elevated temperatures, high

pH, and an excess of  $H_2O_2$  as the oxidant, which also has transportation and storage issues.<sup>8,9</sup> Hence, there is a strong desire for an alternative strategy to produce cyclohexanone oxime under mild conditions.

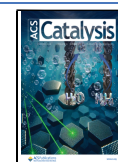
Electrosynthesis stands out as a promising synthetic strategy to enable the sustainable production of chemical feedstocks and added-value compounds by driving reactions under ambient conditions, using electrons generated from renewable electricity instead of redox reagents.<sup>10–14</sup> Particularly, electrochemical nitrate reduction ( $NO_3R$ ) has been demonstrated as a sustainable synthetic approach to upgrade nitrate waste into  $NH_3$ , a very important chemical building block, thus contributing to abating the global nitrogen cycle imbalance.<sup>15–23</sup> Furthermore, a series of surface-adsorbed reaction intermediates have been identified in the  $NO_3R$  to ammonia, such as  $*NO$ ,  $*NH_2OH$ , and  $*NH_2$ , which exhibit high

**Received:** November 8, 2023

**Revised:** February 6, 2024

**Accepted:** February 7, 2024

**Published:** February 15, 2024



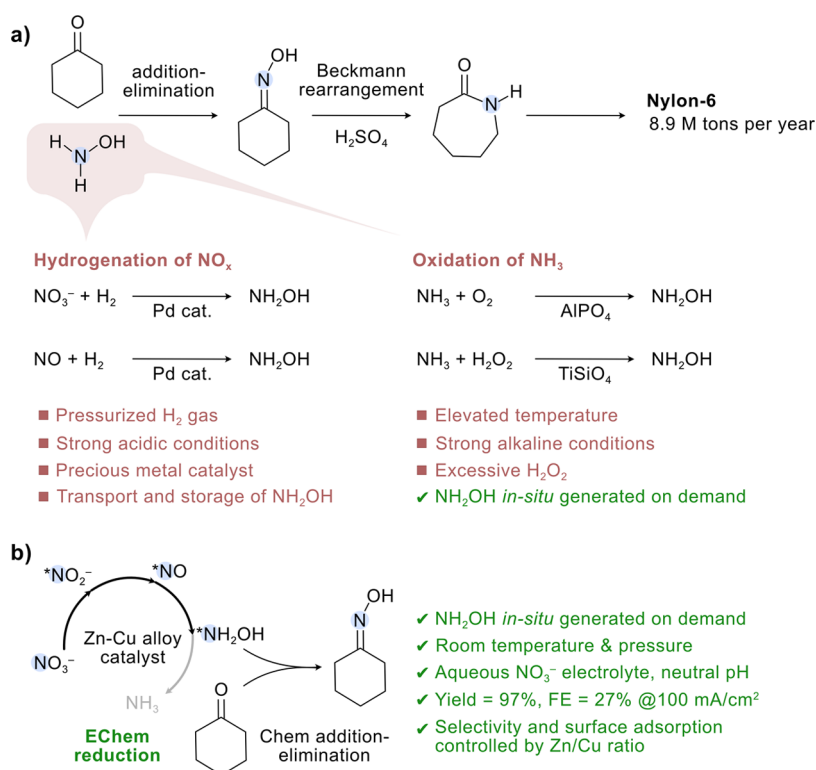


**Figure 1.** Developments in the synthesis of cyclohexanone oxime via thermal and electrochemical methods. (a) Current technologies to synthesize cyclohexanone oxime from cyclohexanone and hydroxylamine, wherein hydroxylamine production is limited by the harsh reaction conditions. (b) Electrosynthesis of cyclohexanone oxime via nitrate reduction under ambient conditions developed in this work. The surface-adsorbed  $\text{*NH}_2\text{OH}$  intermediate generated through the electrochemical reduction of nitrate on a Zn–Cu alloy catalyst can undergo a chemical addition–elimination reaction with the cyclohexanone present in the electrolyte to produce oxime.

nucleophilic reactivities and therefore can be coupled with chemical reactions to build C–N bonds.<sup>24,25</sup> In particular, the electrochemical coreduction of  $\text{CO}_2$  and  $\text{NO}_3^-$  has been reported as an attractive route to produce organonitrogen compounds, including urea, methylamine, and glycine.<sup>26–30</sup> Recently, the Zhang and Tan groups have also shown that the  $\text{*NH}_2$  intermediate generated during  $\text{NO}_3\text{R}$  can interact with  $\text{CO}_2$ -derived compounds (i.e., formic acid or CO) to produce formamide.<sup>31,32</sup> Despite these distinctive methods, current studies on C–N bond formation via  $\text{NO}_3\text{R}$  mainly focus on coupling  $\text{NO}_3\text{R}$  intermediates with  $\text{C}_1$ – $\text{C}_2$  molecules (e.g.,  $\text{CO}_2$ , CO, formic acid, oxalic acid). There are a few recent reports on electrochemical  $\text{NO}_3\text{R}$  systems, which can build C–N bonds in larger organic molecules (i.e.,  $\text{C}_{3+}$  compounds), such as amino acid<sup>33,34</sup> and oxime.<sup>35–38</sup> However,  $\text{NO}_3\text{R}$  can generate a variety of N-containing byproducts (e.g.,  $\text{N}_2$ ,  $\text{NH}_3$ ,  $\text{N}_2\text{O}$ ,  $\text{NO}_2^-$ ), and therefore the understanding of the intricate  $\text{NO}_3\text{R}$  reaction pathways and the controlling of N selectivity toward the desired organonitrogen products remain elusive. Furthermore, the adsorption of N species on the electrocatalyst surface, which plays a central role in tuning the product selectivity, is still largely unexplored for building C–N bonds in  $\text{C}_{3+}$  molecules.

Previous reports revealed that the surface-adsorbed  $\text{*NH}_2\text{OH}$  is a key intermediate in the  $\text{NO}_3\text{R}$  to  $\text{NH}_3$ .<sup>17,18,28,39,40</sup> Recently, the groups of Zhang, Zou, and Li have also independently reported that the  $\text{*NH}_2\text{OH}$  intermediate produced during the electrochemical reduction of  $\text{NO}_3^-/\text{NO}_2^-/\text{NO}$  can undergo a C–N coupling reaction to form oxime.<sup>36–38</sup> Herein, we report a two-step electro-

chemical-chemical (EChem–Chem) process for the one-pot synthesis of cyclohexanone oxime with aqueous nitrate as the N source (Figure 1b) and provide an in-depth investigation of how the product selectivity is controlled by the surface adsorption of N species. A series of Zn–Cu alloys are prepared to drive the electrochemical  $\text{NO}_3\text{R}$  step and generate  $\text{*NH}_2\text{OH}$ , which can then undergo a chemical reaction with cyclohexanone in solution to produce oxime. Through a combination of experimental and computational studies, we demonstrate that the binding of the reaction intermediates on the electrocatalyst surface plays a central role in the EChem–Chem process. Particularly, we show that weak surface adsorption (e.g., on a pure Zn catalyst) can lead to high potentials for the EChem step, whereas strong adsorption (e.g., on a pure Cu catalyst) can promote this process at lower potentials but results in the complete reduction of  $\text{*NH}_2\text{OH}$  to  $\text{NH}_3$  instead of forming oxime. Notably, we find that a Zn–Cu alloy catalyst with an optimized composition of  $\text{Zn}_{93}\text{Cu}_7$  can efficiently convert aqueous  $\text{NO}_3^-$  (pH 7.0) and cyclohexanone into cyclohexanone oxime with a yield of  $97 \pm 2\%$  and a Faradaic efficiency (FE) of  $27 \pm 2\%$  at 100 mA/cm<sup>2</sup>. The  $\text{NH}_2\text{OH}$ -mediated reaction pathway and the relationship between oxime-making activity and surface adsorption are supported by *in situ* Raman spectroscopy and theoretical calculations. Altogether, this work represents a novel strategy for the one-pot electrosynthesis of cyclohexanone oxime from aqueous  $\text{NO}_3^-$  under ambient conditions, which can upgrade  $\text{NO}_3^-$  and enable sustainable organic synthesis. This study also highlights the potential of producing value-added organonitrogen compounds via electrochemical  $\text{NO}_3\text{R}$  as well as the

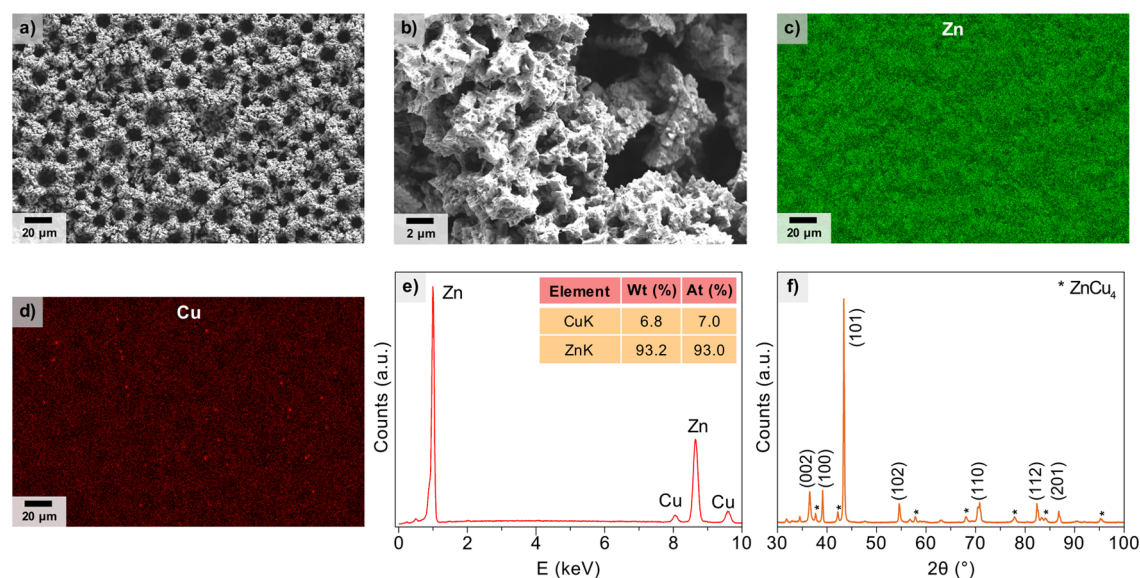


**Figure 2.** Structural characterization of the  $\text{Zn}_{93}\text{Cu}_7$  electrocatalyst. (a, b) SEM images at different magnifications. (c) EDX mapping for Zn. (d) EDX mapping for Cu. (e) EDX quantitative elemental analysis. (f) XRD pattern. The planes in brackets are attributed to Zn (JCPDS 04–0831) and the planes with stars correspond to  $\text{ZnCu}_4$  phase (JCPDS65–6066).

importance of controlling the binding of surface species for product selectivity in electrocatalysis.

## RESULTS AND DISCUSSION

**Preparation and Structural Characterization of the  $\text{Zn}_{93}\text{Cu}_7$  Electrocatalyst.** A  $\text{Zn}_{93}\text{Cu}_7$  electrocatalyst was prepared via electrodeposition. Previous reports have demonstrated that electrodeposition of metal precursors in acid solution can generate metal films (e.g., Cu, Ag, Pd, Zn, and Sn) with highly porous surface caused by the formation of  $\text{H}_2$  bubbles during the process, known as the dynamic hydrogen bubble template (DHBT) approach.<sup>41–43</sup> Here, we utilize the DHBT method to prepare a Zn–Cu alloy catalyst, where  $\text{Zn}^{2+}$  and  $\text{Cu}^{2+}$  precursors ( $\text{Zn}^{2+}/\text{Cu}^{2+}$  ratio = 60) in aqueous acidic solution were electrochemically reduced and deposited onto a Cu foil substrate to form an alloy film (see [Supporting Information](#)). Scanning electron microscopy (SEM) of the Zn–Cu alloy (Figure 2a,b) showed a uniform microporous morphology that is typically observed in metal films prepared by DHBT.

Energy-dispersive X-ray (EDX) mapping showed a homogeneous elemental distribution of Zn and Cu in the sample (Figure 2c,d), indicating the successful formation of an alloy. Furthermore, EDX quantitative analysis revealed a composition of 93 atom % and 7 atom % for Zn and Cu, respectively (Figure 2e). Inductively coupled plasma optical emission spectrometry (ICP-OES) showed a similar elemental composition for the bulk catalyst of 91% Zn and 9% Cu (Table S1). As the electrocatalytic activity and reaction pathway are mainly determined by the surface composition, instead of bulk composition, hereafter we refer to this alloy as  $\text{Zn}_{93}\text{Cu}_7$ . The successful formation of the alloy was also confirmed by X-ray diffraction (XRD), which mainly exhibited crystal planes of pure Zn and minor peaks of a  $\text{ZnCu}_4$  phase (Figure 2f), with no evidence of pure Cu. Hence, the XRD results indicate that Cu was homogeneously distributed within the Zn matrix, in agreement with EDX mapping.

**Electrosynthesis of Cyclohexanone Oxime by  $\text{Zn}_{93}\text{Cu}_7$ .** The  $\text{Zn}_{93}\text{Cu}_7$  alloy (surface area =  $1 \text{ cm}^2$ ) was

used as working electrode to drive the electrochemical  $\text{NO}_3\text{R}$  to produce cyclohexanone oxime in 16 mL of 0.5 M aqueous potassium phosphate (KPi) buffer solution (pH 7.0) containing 100 mM  $\text{KNO}_3$  and 25 mM cyclohexanone. Pt and Ag/AgCl electrodes were used as counter and reference electrodes, respectively, and electrochemical tests were carried out in a gastight H-type cell at constant current (chronopotentiometry). More details of the electrochemical cell setup can be found in Experimental methods and Figure S1. Electrolysis time was adjusted to keep a constant value of charges injected into the electrolyte. The potential required to achieve a certain current density was obtained from the steady-state potential of the electrolysis. A chronopotentiometry graph for electrolysis over 2.5 h at  $100 \text{ mA/cm}^2$  can be found in Figure S2 as an example of obtaining the steady-state potential.

The liquid reaction mixture was analyzed by nuclear magnetic resonance (NMR) to identify the organic compounds present. The recorded  $^1\text{H}$  NMR spectra before and after electrolysis, shown in Figure 3a, indicate that the cyclohexanone peaks almost disappeared after the reaction, while new peaks aligned with pure cyclohexanone oxime emerged, confirming the successful conversion of cyclohexanone into cyclohexanone oxime. The  $^{13}\text{C}$  NMR spectrum obtained for the reaction mixture after electrolysis also supported the formation of cyclohexanone oxime (Figure 3b).

The production of cyclohexanone oxime was further confirmed by mass spectroscopy (MS, Figure S3). The reaction mixture was also analyzed by high-performance liquid chromatography (HPLC) to quantify cyclohexanone and cyclohexanone oxime (Figure S4) as well as ion chromatography (IC) to detect and quantify different nitrogen species in solution, namely,  $\text{NO}_3^-$ ,  $\text{NO}_2^-$ , and  $\text{NH}_3$  (Figure S5). In addition, the gas sample in the headspace of the H-cell was analyzed by gas chromatography (GC). Details of products characterization can be found in the [Supporting Information](#).

The FE and steady-state potential for the electrochemical  $\text{NO}_3\text{R}$  were measured at constant current densities of 5, 25, 50, 100, and  $150 \text{ mA/cm}^2$ , the results of which are summarized in Figure 3c. At  $5 \text{ mA/cm}^2$ , a small amount of cyclohexanone

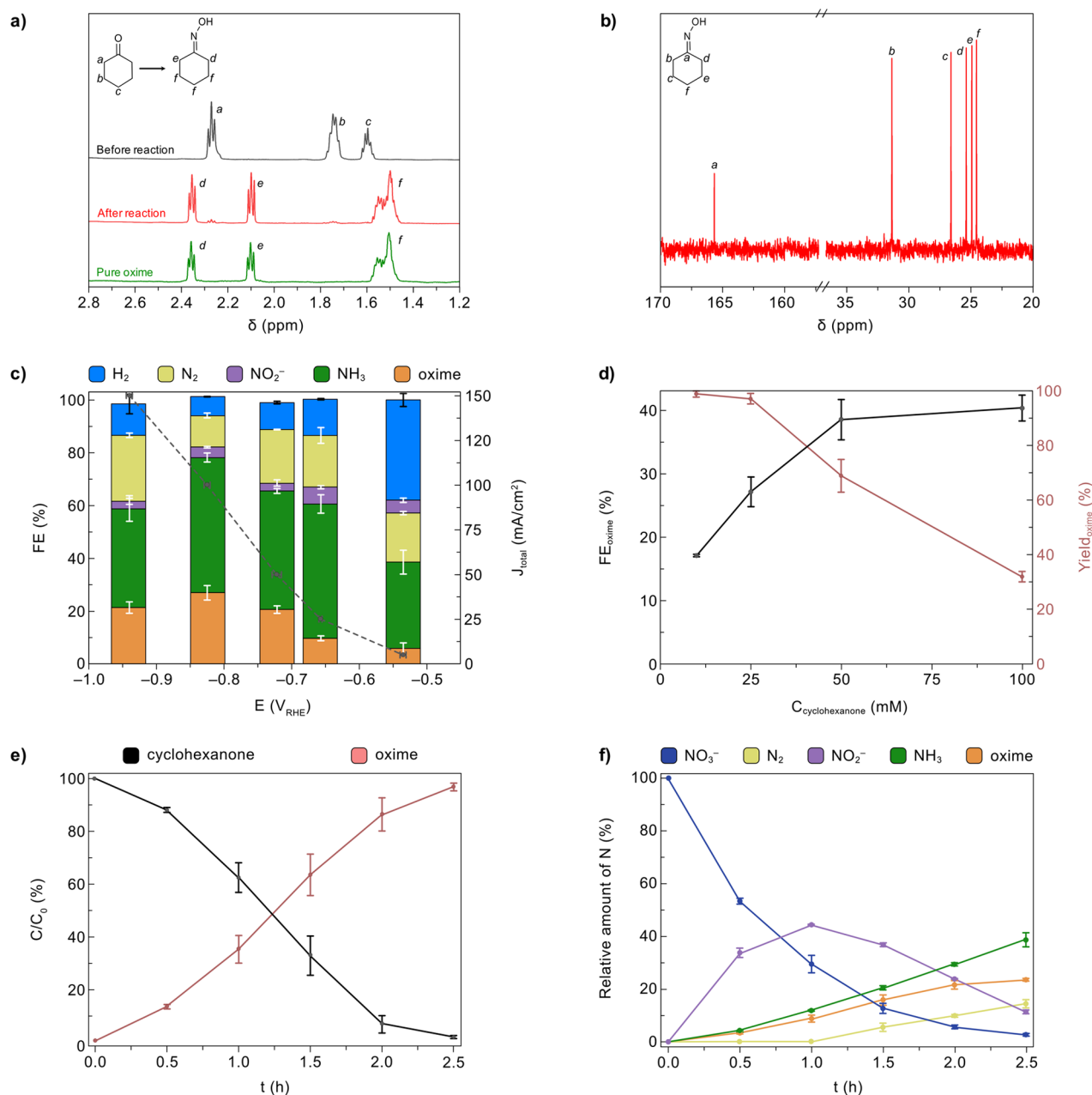


**Figure 3.** Electrosynthesis of cyclohexanone oxime from  $\text{NO}_3^-$  and cyclohexanone driven by a  $\text{Zn}_{93}\text{Cu}_7$ -electrocatalyst. (a)  $^1\text{H}$  NMR spectra for the reaction mixture before and after 2.5 h electrolysis, and pure cyclohexanone oxime as control. (b)  $^{13}\text{C}$  NMR spectra for the reaction mixture for constant current electrolysis. (c) FE and total current density ( $J_{\text{total}}$ ) at different potentials. Potential values were obtained from the steady-state potentials for constant current electrolysis. (d) FE and yield of cyclohexanone oxime measured at 100  $\text{mA}/\text{cm}^2$  with different concentrations of cyclohexanone added into 100 mM  $\text{KNO}_3$  electrolyte. (e) Conversion of cyclohexanone into cyclohexanone oxime over 2.5 h of electrolysis at 100  $\text{mA}/\text{cm}^2$ . (f) Relative amount of nitrogen products over 2.5 h of electrolysis at 100  $\text{mA}/\text{cm}^2$ . Reaction conditions:  $\text{Zn}_{93}\text{Cu}_7$  cathode (surface area = 1  $\text{cm}^2$ ) immersed in 16 mL of aqueous buffer solution (0.5 M KPi, pH 7.0) containing 100 mM  $\text{KNO}_3$  and 25 mM cyclohexanone. Error bars correspond to the standard deviation of triplicate experiments.

oxime was detected (FE =  $6 \pm 2\%$ ), while the major products were  $\text{NH}_3$  and  $\text{H}_2$ . The FE for cyclohexanone oxime increased to  $27 \pm 2\%$  at 100  $\text{mA}/\text{cm}^2$  and  $-0.82$  V vs reversible hydrogen electrode ( $V_{\text{RHE}}$ ) and then decreased to  $21 \pm 2\%$  when the current density further increased to 150  $\text{mA}/\text{cm}^2$ . At the different current densities investigated in this work,  $\text{NH}_3$  was generated as the major product with FEs between 30 and 50%; other detected products included  $\text{NO}_2^-$ ,  $\text{N}_2$ , and  $\text{H}_2$ .

The influence of different concentrations of cyclohexanone (i.e., 10, 25, 50, 100 mM;  $\text{NO}_3^-$  concentration was kept

constant at 100 mM) added to the electrolyte was investigated through 2.5 h electrolysis experiments at 100  $\text{mA}/\text{cm}^2$  (Figure 3d). Low concentrations of cyclohexanone (e.g., 10 mM) were found to produce cyclohexanone oxime with high yields ( $99 \pm 1\%$ ), while the FE for cyclohexanone oxime was quite low ( $17 \pm 0.3\%$ ). In contrast, high concentrations of cyclohexanone (e.g., 100 mM) led to high FE for cyclohexanone oxime ( $40 \pm 2\%$ ), but the yield was lower ( $32 \pm 2\%$ ). Therefore, a medium concentration of cyclohexanone (25 mM) was chosen to balance the yield and FE for cyclohexanone oxime.

Table 1. Control Experiments for Cyclohexanone Oxime Production

entry	cathode	C source	N source	electrolysis	cyclohexanone oxime?
1	Zn <sub>93</sub> Cu <sub>7</sub>	cyclohexanone	KNO <sub>3</sub>	yes	yes
2	Zn <sub>93</sub> Cu <sub>7</sub>	cyclohexanone	KNO <sub>3</sub>	no	no
3	Zn <sub>93</sub> Cu <sub>7</sub>	cyclohexanone	KNO <sub>3</sub>	yes	no
4	Zn <sub>93</sub> Cu <sub>7</sub>	cyclohexanone	KNO <sub>3</sub>	yes	no
5	Cu foil	cyclohexanone	KNO <sub>3</sub>	yes	no
6	Zn <sub>93</sub> Cu <sub>7</sub>	cyclohexanone	K <sup>15</sup> NO <sub>3</sub>	yes	yes, <sup>15</sup> N-labeled
7	Zn <sub>93</sub> Cu <sub>7</sub>	cyclohexanone	KNO <sub>2</sub>	yes	yes
8	Zn <sub>93</sub> Cu <sub>7</sub>	cyclohexanone	NO	yes	yes
9	Zn <sub>93</sub> Cu <sub>7</sub>	cyclohexanone	NH <sub>2</sub> OH	yes	yes
10	Zn <sub>93</sub> Cu <sub>7</sub>	cyclohexanone	NH <sub>3</sub>	yes	no

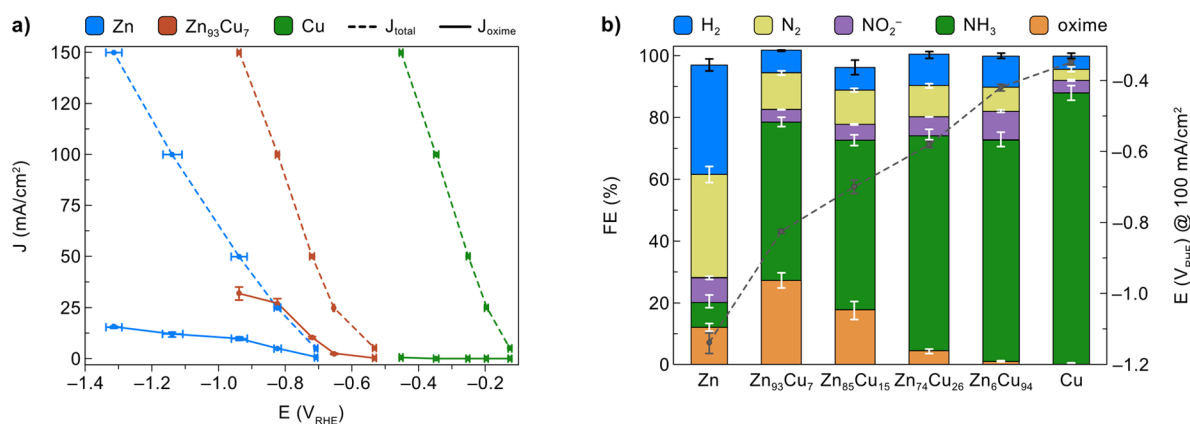


**Figure 4.** Production of cyclohexanone oxime from NO<sub>3</sub><sup>-</sup> and cyclohexanone driven by different Zn/Cu electrocatalysts. (a) Total current density ( $J_{total}$ ) and partial current density for cyclohexanone oxime ( $J_{oxime}$ ) at different potentials for Zn, Zn<sub>93</sub>Cu<sub>7</sub>, and Cu electrocatalysts. (b) FE and potential required to achieve  $J_{total}$  at 100 mA/cm<sup>2</sup> with different Zn/Cu electrocatalysts. Reaction conditions: Zn/Cu cathode (surface area = 1 cm<sup>2</sup>) immersed in 16 mL of aqueous buffer solution (0.5 M KPi, pH 7.0) containing 100 mM KNO<sub>3</sub> and 25 mM cyclohexanone. Potential values were obtained from the steady-state potentials for constant current electrolysis. Error bars correspond to the standard deviation of triplicate experiments.

After optimizing the reaction conditions as 100 mA/cm<sup>2</sup> and 25 mM cyclohexanone, we next monitored the temporal changes in the concentrations of the reactants and products by analyzing reaction aliquots every 30 min over 2.5 h of electrolysis. As shown in Figure 3e, oxime was produced with  $97 \pm 2\%$  yield and the ketone reactant was almost fully converted after 2.5 h (conversion  $\sim 98\%$ ), which is consistent with the recorded <sup>1</sup>H NMR spectrum. These results also demonstrated a high carbon selectivity which is close to 100%, while the nitrogen selectivity was investigated by monitoring the relative amounts of all nitrogen compounds over the 2.5 h electrolysis (Figure 3f). The NO<sub>3</sub><sup>-</sup> reactant was first converted into NO<sub>2</sub><sup>-</sup>, which achieved a maximum yield of ca. 45% after 1 h, indicating that NO<sub>2</sub><sup>-</sup> is a reaction intermediate, in line with previous reports.<sup>15–20,44</sup> After 2.5 h of electrolysis, ca. 3% NO<sub>3</sub><sup>-</sup> and 15% NO<sub>2</sub><sup>-</sup> remained in solution, while cyclohexanone oxime and NH<sub>3</sub> were the main species produced in ca. 24% and 40% yields, respectively. Under these conditions, N<sub>2</sub> was generated as a byproduct ( $\sim 15\%$ ), which is consistent with previous NO<sub>3</sub>R studies driven by Zn-rich electrocatalysts.<sup>45–47</sup> Importantly, the surface structures of the Zn<sub>93</sub>Cu<sub>7</sub> electrocatalyst remained stable after three tests of 2.5 h electrolysis (Figures S6 and S7), and the electrocatalyst could be reused to produce cyclohexanone oxime with similar FEs compared to the initial test (Figure S8).

Next, a series of control experiments were performed to confirm the C and N sources and shed light into the reaction pathway (Table 1). As expected, the reaction in the absence of

electrolysis or cyclohexanone or NO<sub>3</sub><sup>-</sup> did not yield any oxime product (entries 2, 3 and 4). Experiments using bare Cu foil as the cathode (entry 5) were also inactive toward oxime formation, highlighting the catalytic role of the Zn<sub>93</sub>Cu<sub>7</sub> alloy. To confirm the N source, an isotopic labeling experiment with K<sup>15</sup>NO<sub>3</sub> was carried out (entry 6), and the formation of <sup>15</sup>N-labeled cyclohexanone oxime was corroborated by mass spectroscopy (Figure S9). The recorded <sup>1</sup>H NMR spectrum (Figure S9) also revealed the duplet splitting behavior of the <sup>15</sup>NH<sub>4</sub><sup>+</sup> peak generated from <sup>15</sup>NO<sub>3</sub><sup>-</sup> reduction, while <sup>14</sup>NH<sub>4</sub><sup>+</sup> produced by normal <sup>14</sup>NO<sub>3</sub><sup>-</sup> reduction features a triplet peak. A series of possible NO<sub>3</sub>R intermediates, including NO<sub>2</sub><sup>-</sup>, NO, and NH<sub>2</sub>OH, was each used as the starting N source (entries 7–9) and resulted in the formation of cyclohexanone oxime, indicating a NO<sub>3</sub>R reaction pathway via those species that is consistent with previous studies.<sup>17,18,28</sup> Finally, using NH<sub>3</sub> as the N source (entry 10) failed to produce any cyclohexanone oxime, further confirming that the oxime product was generated from an intermediate of NO<sub>3</sub>R instead of the final product of NO<sub>3</sub>R (NH<sub>3</sub>).

**Electrosynthesis of Cyclohexanone Oxime by Different Zn–Cu Alloys.** Pure Zn and Cu electrocatalysts were also prepared through similar DHBT electrodeposition methods to compare their catalytic performance with that of the Zn<sub>93</sub>Cu<sub>7</sub> alloy. The X-ray photoelectron spectroscopy (XPS) analysis revealed that the Zn/Cu catalysts were mainly in metallic phases while a small portion of metal oxide was formed due to the inevitable surface oxidation of the catalysts in the

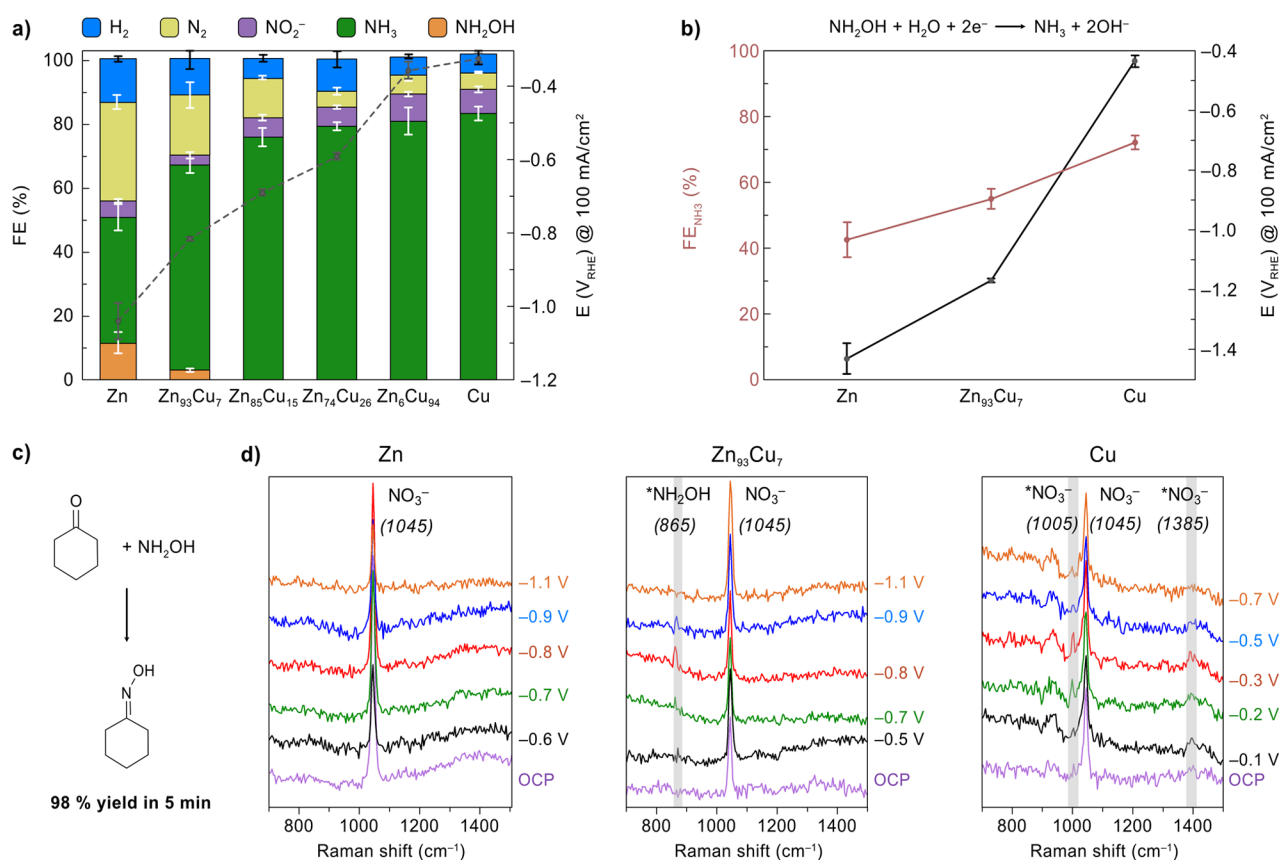


**Figure 5.** Mechanistic study of the NO<sub>3</sub>R process mediated by surface-adsorbed NH<sub>2</sub>OH. (a) Electroreduction of NO<sub>3</sub><sup>-</sup> (without cyclohexanone) at 100 mA/cm<sup>2</sup> with different Zn–Cu alloy catalysts. (b) Electroreduction of NH<sub>2</sub>OH to NH<sub>3</sub> at 100 mA/cm<sup>2</sup> for Zn, Zn<sub>93</sub>Cu<sub>7</sub> and Cu. Reaction conditions: Zn/Cu cathode (surface area = 1 cm<sup>2</sup>) immersed in 16 mL aqueous buffer solution (0.5 M KPi, pH 7.0) containing 100 mM KNO<sub>3</sub> (for a) or NH<sub>2</sub>OH (for b). Error bars correspond to the standard deviation of triplicate experiments. (c) Chemical addition–elimination reaction between cyclohexanone and NH<sub>2</sub>OH to yield cyclohexanone oxime. Reaction conditions: 16 mL aqueous solution containing 25 mM cyclohexanone and 25 mM NH<sub>2</sub>OH. (d) *In situ* Raman spectra for electrochemical NO<sub>3</sub>R (without cyclohexanone) recorded at different potentials (vs RHE) on pure Zn, Zn<sub>93</sub>Cu<sub>7</sub> alloy, and pure Cu electrocatalysts. The peak at 1045 cm<sup>-1</sup> was consistently observed for the NO<sub>3</sub><sup>-</sup> in solution. The asterisk in the labeled species denote an adsorbed state, e.g., \*NH<sub>2</sub>OH, \*NO<sub>3</sub><sup>-</sup>.

atmosphere (Figure S10). The SEM images and XRD results for pure Zn and Cu catalysts are also shown in Figures S11 and S12. As displayed in Figure 4a, pure Cu required a significantly lower potential than pure Zn to achieve the same total current density ( $J_{\text{total}}$ , top), while the Zn<sub>93</sub>Cu<sub>7</sub> alloy showed an intermediate behavior, suggesting that the electrochemical NO<sub>3</sub>R is more favorable on Cu. However, pure Cu could barely produce any cyclohexanone oxime, whereas pure Zn was capable of forming cyclohexanone oxime. Notably, Zn<sub>93</sub>Cu<sub>7</sub> attained an even higher partial current density for oxime ( $J_{\text{oxime}}$ , bottom) at a significantly lower potential compared to pure Zn. For example, a  $J_{\text{oxime}}$  of  $32 \pm 3$  mA/cm<sup>2</sup> was achieved at  $-0.94$  V<sub>RHE</sub> on Zn<sub>93</sub>Cu<sub>7</sub>, compared to  $10 \pm 1$  mA/cm<sup>2</sup> on pure Zn.

Although pure Cu itself was deemed inactive toward cyclohexanone oxime production, the introduction of a small percentage (7%) of Cu into Zn resulted in a significantly enhanced performance. Hence, to investigate how Zn/Cu composition influences NO<sub>3</sub>R, a series of Zn–Cu alloy catalysts were prepared by electrodeposition using precursor solutions with different Zn/Cu ratios (see Table S1 for details). The bulk composition was measured by ICP-OES analysis (Table S1). EDX analysis of the surface elemental composition (Figure S13), which is more related to the electrocatalytic activity, determined the surface composition of these samples to be Zn<sub>93</sub>Cu<sub>7</sub>, Zn<sub>85</sub>Cu<sub>15</sub>, Zn<sub>74</sub>Cu<sub>26</sub>, and

Zn<sub>6</sub>Cu<sub>94</sub>. Subsequently, the Zn–Cu alloys were tested for NO<sub>3</sub>R at 100 mA/cm<sup>2</sup>, with the measured potentials and FEs summarized in Figure 4b. As the Cu content increased, the NO<sub>3</sub>R could be driven at lower potentials and the FE for NH<sub>3</sub> was significantly enhanced, consistent with previous reports that Cu is an efficient electrocatalyst for NO<sub>3</sub><sup>-</sup> to NH<sub>3</sub> conversion.<sup>15,17,18</sup> However, Cu-rich catalysts (i.e., Zn<sub>6</sub>Cu<sub>94</sub> and pure Cu) resulted in low FEs for cyclohexanone oxime (<1%). The highest FE for the oxime product was achieved on Zn<sub>93</sub>Cu<sub>7</sub> ( $27 \pm 3\%$ ), while pure Zn and Zn<sub>85</sub>Cu<sub>15</sub> produced oxime with lower FEs ( $12 \pm 1\%$  and  $17 \pm 3\%$ , respectively). We also note that pure Zn also produced a substantial amount of N<sub>2</sub> (FE =  $33 \pm 3\%$ ) and H<sub>2</sub> (FE =  $35 \pm 2\%$ ) compared to the other electrocatalysts.

Based on the above experimental results and previous NO<sub>3</sub>R studies<sup>48</sup> that revealed a significantly stronger adsorption of reaction intermediates on Cu compared to Zn, we posited four possible (not excluding) reasons for the different behavior observed with the Zn–Cu alloy electrocatalysts: (1) Cu has a stronger surface adsorption of NO<sub>3</sub><sup>-</sup> than Zn and therefore facilitates the electrochemical NO<sub>3</sub>R at lower potentials; (2) Cu favors the further electroreduction of \*NH<sub>2</sub>OH to NH<sub>3</sub>, instead of the chemical reaction with cyclohexanone to give oxime; (3) introducing Cu into Zn creates a more porous surface morphology and thus leads to lower NO<sub>3</sub>R potentials;

(4) pure Zn is disadvantaged by the competing  $\text{NO}_3\text{R}$  pathway toward  $\text{N}_2$ , rather than  $\text{NH}_2\text{OH}$  or  $\text{NH}_3$ . The difference in surface morphology for Zn, Cu, and  $\text{Zn}_{93}\text{Cu}_7$  is supported by SEM images (Figure S11) and the measurements of the electrochemical active surface area (ECSA, Figure S14). Hence, we next carried out further experimental and theoretical studies to prove the other three possible reasons.

**Experimental Mechanistic Studies.** The detection of the  $\text{NH}_2\text{OH}$  intermediate proved very challenging in the presence of cyclohexanone because of the extremely fast nucleophilic addition of  $\text{NH}_2\text{OH}$  to the ketone. Therefore, we set out to perform electrochemical  $\text{NO}_3\text{R}$  experiments with the different Zn/Cu catalysts in the absence of cyclohexanone to confirm the formation of  $\text{NH}_2\text{OH}$ . As shown in Figure 5a, similar trends of lower potentials and higher FE toward  $\text{NH}_3$  were observed as the Cu content increased, consistent with hypothesis 1 that Cu facilitates electrochemical  $\text{NO}_3\text{R}$ . More importantly, pure Zn and  $\text{Zn}_{93}\text{Cu}_7$  were found to produce  $\text{NH}_2\text{OH}$  at 100  $\text{mA}/\text{cm}^2$  with FEs of  $12 \pm 3\%$  and  $3 \pm 1\%$ , respectively (detection of  $\text{NH}_2\text{OH}$  in solution is shown in Figure S15). Pure Zn can produce more  $\text{NH}_2\text{OH}$  than  $\text{Zn}_{93}\text{Cu}_7$  in the absence of cyclohexanone because the  $^*\text{NH}_2\text{OH}$  produced on  $\text{Zn}_{93}\text{Cu}_7$  can be further reduced to  $\text{NH}_3$  when cyclohexanone is unavailable (see below discussion that  $\text{Zn}_{93}\text{Cu}_7$  is a better  $\text{NH}_2\text{OH}$  electroreduction catalyst than pure Zn). Conversely, in the presence of cyclohexanone,  $\text{Zn}_{93}\text{Cu}_7$  gave more oxime because the addition of cyclohexanone shifts the equilibrium toward cyclohexanone oxime formation, outcompeting  $^*\text{NH}_2\text{OH}$  reduction. The formation of  $^*\text{NH}_2\text{OH}$  and its subsequent release into the electrolyte solution were also evidenced at other current densities for  $\text{Zn}_{93}\text{Cu}_7$  (Figure S16). In contrast, the other electrocatalysts with higher Cu contents did not yield any detectable amount of  $\text{NH}_2\text{OH}$ , indicating that this intermediate can be further reduced to  $\text{NH}_3$  on Cu-rich catalysts, whereas on Zn-rich catalysts (i.e., pure Zn and  $\text{Zn}_{93}\text{Cu}_7$ ) the  $^*\text{NH}_2\text{OH}$  intermediate can desorb from the surface and accumulate in the solution to a detectable concentration.

To further understand the interaction of  $\text{NH}_2\text{OH}$  with the electrocatalyst surface, the electroreduction of  $\text{NH}_2\text{OH}$  to  $\text{NH}_3$  was investigated on pure Zn,  $\text{Zn}_{93}\text{Cu}_7$ , and pure Cu (Figure 5b). Experiments with pure Cu led to a significantly higher FE for  $\text{NH}_3$  and a lower potential compared to pure Zn and  $\text{Zn}_{93}\text{Cu}_7$ , demonstrating that the electroreduction of  $\text{NH}_2\text{OH}$  to  $\text{NH}_3$  is much more favorable on the Cu surface compared to Zn. The central role of  $\text{NH}_2\text{OH}$  in the production of oxime was further confirmed by mixing cyclohexanone and  $\text{NH}_2\text{OH}$  in solution without electrolysis, which readily produced cyclohexanone oxime with 98% yield after only 5 min (Figure 5c). The fast kinetics and favorable thermodynamics of this noncatalytic addition–elimination reaction ensures effective C–N bond formation. Given that  $\text{NH}_2\text{OH}$  is the most nucleophilic species among all the proposed  $\text{NO}_3\text{R}$  intermediates and the widely known nucleophilic addition of  $\text{NH}_2\text{OH}$  to ketones,<sup>28</sup> we concluded that  $\text{NH}_2\text{OH}$  is the  $\text{NO}_3\text{R}$  intermediate that reacts with cyclohexanone to generate oxime. These results collectively support hypothesis 2 that, on Zn-rich electrocatalysts, the electrochemically generated  $\text{NH}_2\text{OH}$  tends to undergo a subsequent chemical reaction with cyclohexanone to produce oxime rather than being further reduced to  $\text{NH}_3$ .

Further insights were obtained by analyzing the surface-adsorbed species during electrochemical  $\text{NO}_3\text{R}$  at different

potentials by *in situ* Raman spectroscopy (Figure 5d). Experiments with pure Zn showed a single Raman peak at  $1045\text{ cm}^{-1}$ , which was attributed to the  $\text{NO}_3^-$  in solution<sup>49,50</sup> (a control experiment with an aqueous  $\text{KNO}_3$  solution in absence of electrocatalyst also showed the peak at  $1045\text{ cm}^{-1}$ ). On the other hand, for  $\text{Zn}_{93}\text{Cu}_7$ , a small peak at  $865\text{ cm}^{-1}$  was observed at  $-0.5\text{ V}_{\text{RHE}}$ , which gradually grew as the potential increased to  $-0.8\text{ V}_{\text{RHE}}$  before disappearing at  $-1.1\text{ V}_{\text{RHE}}$ . This peak can be attributed to the N–O stretch mode of surface-adsorbed  $^*\text{NH}_2\text{OH}$  intermediate,<sup>49,51</sup> providing direct experimental evidence for this species on the  $\text{Zn}_{93}\text{Cu}_7$  surface. This observation also confirms hypothesis 2 that  $\text{Zn}_{93}\text{Cu}_7$  can generate  $^*\text{NH}_2\text{OH}$  intermediate which plays a central role in the reaction. In contrast, the pure Cu electrocatalyst exhibited two peaks at 1005 and  $1385\text{ cm}^{-1}$  corresponding to adsorbed  $^*\text{NO}_3^-$  species,<sup>49,50</sup> which grew with the potential increasing to  $-0.3\text{ V}_{\text{RHE}}$  and then disappeared at more negative potentials. The absence of the  $^*\text{NH}_2\text{OH}$  peak on pure Cu can be explained by the favored further reduction of  $^*\text{NH}_2\text{OH}$  into  $\text{NH}_3$  on Cu. The absence of a clear Raman peak for the adsorbed  $^*\text{NH}_2\text{OH}$  on pure Zn can be explained by the weak adsorption of  $^*\text{NH}_2\text{OH}$  on Zn, which makes the surface-adsorbed intermediates difficult to be observed by a surface-enhanced technique. Overall, these observations on pure Cu and the absence of adsorbed species on pure Zn collectively support hypothesis 1 that Cu provides a stronger binding for  $\text{NO}_3^-$  compared to Zn, which is beneficial for electrochemical  $\text{NO}_3\text{R}$ .

**Computational Mechanistic Studies.** To shed further light on the different  $\text{NO}_3\text{R}$  selectivities toward  $\text{NH}_2\text{OH}$ ,  $\text{NH}_3$ , and  $\text{N}_2$  observed with the Cu, Zn, and  $\text{Zn}_{93}\text{Cu}_7$  electrocatalysts, we performed a mechanistic investigation by means of periodic density functional theory (DFT) calculations (see the Supporting Information for details). To avoid the well-documented issues associated with the modeling of charged species through the introduction of a background charge in the unit cell,<sup>52,53</sup> and since the reduction from  $\text{NO}_3^-$  to nitric oxide (NO) is widely understood,<sup>15,37,52–54</sup> we set the zero of energies in our calculations to be the neutral NO molecule instead of  $\text{NO}_3^-$  (see the Supporting Information for further details).

To study the  $\text{NO}_3\text{R}$  reactivity on the different electrocatalysts, we constructed Cu(111), Zn(101), and  $\text{Zn}_{93}\text{Cu}_7$ (101) surface slab models (as confirmed by XRD in Figure 2f and Figure S12) followed by the assessment of their surface coverages under experimental conditions,<sup>55,56</sup> as depicted in Figure S17. For Cu(111), DFT simulations predict 75% of the *fcc* sites to be covered by H atoms, while all the *bridge* positions on Zn(101) and  $\text{Zn}_{93}\text{Cu}_7$ (101) are occupied by H. Taking these surface terminations as the catalyst resting state, the electroreduction of NO to  $\text{N}_2$ ,  $\text{NH}_2\text{OH}$ , and  $\text{NH}_3$  was then explored via a series of proton-coupled electron transfer (PCET) steps, as reported elsewhere.<sup>17,18,28</sup> Furthermore, at each step, the hydrogenation of both the N and O atoms was considered as well as all the possible adsorption sites for each reaction intermediate (see Tables S2 and S3).

First, the  $\text{N}_2$  evolution reaction was investigated via the mechanism outlined below (\* denotes a surface site), which involves the adsorption of NO on the electrode surface, two sequential PCETs at the O atom, and the N–N coupling followed by  $\text{N}_2$  desorption (eqs 1–4).<sup>21,57</sup>





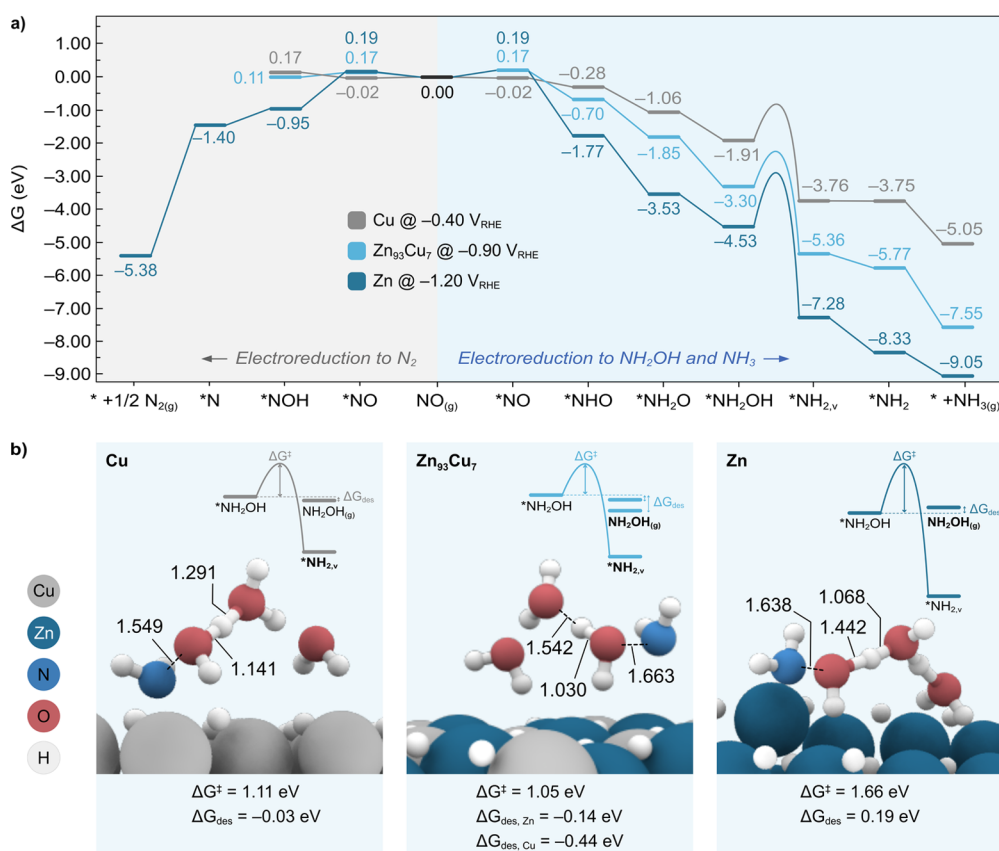


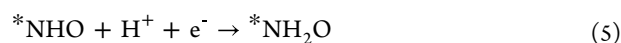
**Figure 6.** Computational mechanistic studies for the formation of N<sub>2</sub>, NH<sub>2</sub>OH, and NH<sub>3</sub>. (a) Gibbs energy diagram for the electroreduction of NO to N<sub>2</sub> (left) and NO to NH<sub>2</sub>OH and NH<sub>3</sub> (right) for the Cu(111), Zn<sub>93</sub>Cu<sub>7</sub>(101) and Zn(101) surfaces at the experimental applied potentials of -0.40, -0.90, and -1.20 V<sub>RHE</sub>, respectively. The label \*NH<sub>2,v</sub> denotes the formation of the \*NH<sub>2</sub> intermediate from \*NH<sub>2</sub>OH by sourcing the H atom from the surface coverage, whereas the label \*NH<sub>2</sub> indicates the same intermediate after replenishing the surface H vacancy. (b) Optimized transition state structures and associated kinetic barriers (ΔG<sup>‡</sup>) for the electroreduction of \*NH<sub>2</sub>OH on pure Cu (left), Zn<sub>93</sub>Cu<sub>7</sub> (middle), and pure Zn (right). This step was modeled with two explicit water molecules to assist H transfer. Relevant bond distances are given in Å. The Gibbs energies associated to \*NH<sub>2</sub>OH desorption (ΔG<sub>des</sub>) are also provided. The insets illustrate the competition between the electroreduction and desorption of \*NH<sub>2</sub>OH. The most favored species are highlighted in bold. Color code: Cu (gray), Zn (dark blue), O (red), N (blue), H (white).



The computed Gibbs energy diagrams on the different electrocatalysts are depicted in Figure 6a (left). These are reported at the experimental potentials where the same total current density of 100 mA/cm<sup>2</sup> can be achieved on the Zn, Cu, and Zn<sub>93</sub>Cu<sub>7</sub> electrocatalysts. These diagrams revealed that the first PCET to form the intermediate \*NOH (i.e., hydrogenated at the O, eq 2) is thermodynamically favorable on pure Zn (i.e., -0.95 eV), whereas this process is slightly endergonic both on pure Cu and Zn<sub>93</sub>Cu<sub>7</sub> (i.e., +0.17 and +0.11 eV, respectively). These findings and the highly exergonic formation of N<sub>2</sub> predicted on Zn (i.e., -5.38 eV) are in line with the higher FE toward N<sub>2</sub> observed in experiments on Zn compared to Cu and Zn<sub>93</sub>Cu<sub>7</sub> (Figure 4b). Hence, theoretical calculations support hypothesis 4 that the formation of NH<sub>2</sub>OH (which eventually produces oxime) on pure Zn is disadvantaged by the competing NO<sub>3</sub>R pathway toward N<sub>2</sub>, which is marginally accessible on Cu and Zn<sub>93</sub>Cu<sub>7</sub>. These results could also explain the lower yields of oxime achieved on pure Zn relative to the Zn<sub>93</sub>Cu<sub>7</sub> alloy (Figure 4b).

The production of NH<sub>2</sub>OH and NH<sub>3</sub> relies instead on the formation of the \*NHO intermediate (i.e., hydrogenated at the N), which is thermodynamically more favorable than \*NOH on all the electrocatalysts investigated in this work (Figure 6a, right). Notably, while DFT calculations predict the generation of both \*NOH and \*NHO on Zn(101) to be essentially irreversible at room temperature due to their associated highly exergonic energies (i.e., -0.95 and -1.77 eV, respectively), for Cu and Zn<sub>93</sub>Cu<sub>7</sub>, only the formation of \*NHO is thermodynamically driven (i.e., -0.28 and -0.70 eV, respectively). Hence, the relative stability between the \*NHO vs \*NOH intermediates and the binding strength of NH<sub>2</sub>OH can be used as descriptors to rationalize product selectivity, as we discuss in detail below.

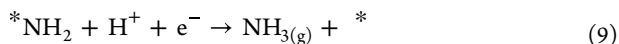
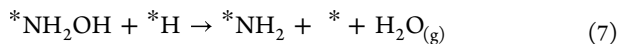
The reduction of \*NHO toward \*NH<sub>2</sub>OH and NH<sub>3</sub> was investigated via a series of PCET steps. According to DFT calculations, the lowest energy pathway for \*NH<sub>2</sub>OH formation involves the sequential hydrogenation of the N and O atoms, as outlined in eqs 5 and 6.



As seen from Figure 6a (right), both processes are exergonic on Zn, Cu, and Zn<sub>93</sub>Cu<sub>7</sub>, supporting the formation of the

\*NH<sub>2</sub>OH intermediate on all these electrocatalysts. In particular, the trend obtained from calculations, from more to less exergonic, is Zn > Zn<sub>93</sub>Cu<sub>7</sub> > Cu.

The subsequent electroreduction of \*NH<sub>2</sub>OH to NH<sub>3</sub> was then examined according to the mechanism shown in eqs 7–9.



Again, calculations predict the electroreduction of \*NH<sub>2</sub>OH to NH<sub>3</sub> to be thermodynamically downhill, in line with the experimental observation of NH<sub>3</sub> with all the studied electrocatalysts (Figures 4b and 5a). However, we note that \*NH<sub>2</sub>OH electroreduction is competing with \*NH<sub>2</sub>OH desorption from the electrode surface, which is followed by a chemical reaction with the cyclohexanone in solution to produce oxime. Therefore, to shed light on the different NH<sub>3</sub>/oxime selectivities observed in experiments, we set out to compute both the thermodynamic driving force for \*NH<sub>2</sub>OH desorption ( $\Delta G_{\text{des}}$ ) and the kinetic barrier for \*NH<sub>2</sub>OH electroreduction ( $\Delta G^\ddagger$ ), the results of which are summarized in Figure 6b. Notably, the \*NH<sub>2</sub>OH desorption is almost thermoneutral on Cu (−0.03 eV), slightly endergonic on Zn (+0.19 eV), and exergonic on the Zn<sub>93</sub>Cu<sub>7</sub> alloy (−0.14 and −0.44 eV from Zn and Cu sites, respectively). For the modeling of the \*NH<sub>2</sub>OH electroreduction, we note that this step involves the hydrogenation of the O atom with the concomitant cleavage of the N–O bond, which can be promoted by either the aqueous electrolyte or the H surface coverage. However, given that the pK<sub>b</sub> of NH<sub>2</sub>OH in water is ca. 8.1,<sup>38</sup> it is unlikely that NH<sub>2</sub>OH will be protonated by the aqueous electrolyte at the experimental pH 7. Hence, we focused on modeling the reaction kinetics of the \*NH<sub>2</sub>OH electroreduction by sourcing a H atom from the electrode surface.<sup>56</sup> Furthermore, because of the relatively large distance between the O lone pairs in \*NH<sub>2</sub>OH and the nearest surface H (ca. 3.0 Å on Cu(111) and ca. 4.2 Å on both Zn<sub>93</sub>Cu<sub>7</sub>(101) and Zn(101)), we envisioned this process to be promoted by the aqueous electrolyte. To capture this in our kinetic studies, we introduced two H<sub>2</sub>O molecules to mediate the H transfer. This led to the following energy barriers for the different electrocatalysts: Cu (1.11 eV) ~ Zn<sub>93</sub>Cu<sub>7</sub> (1.05 eV) < Zn (1.66 eV) (Figure 6b). With these values of  $\Delta G^\ddagger$  and  $\Delta G_{\text{des}}$ , we can now rationalize the NH<sub>3</sub>/oxime selectivities on Cu, Zn<sub>93</sub>Cu<sub>7</sub>, and Zn as follows. On pure Cu, \*NH<sub>2</sub>OH electroreduction (with moderate  $\Delta G^\ddagger$ ) is favored over \*NH<sub>2</sub>OH desorption, rendering NH<sub>3</sub> as the major NO<sub>3</sub>R product. On the other hand, the high  $\Delta G^\ddagger$  found for pure Zn hinders \*NH<sub>2</sub>OH electroreduction, while the slightly endergonic  $\Delta G_{\text{des}}$  allows \*NH<sub>2</sub>OH desorption at room temperature, coherently with the product distribution observed experimentally (Figures 4b and 5a). Finally, on the Zn<sub>93</sub>Cu<sub>7</sub> alloy, the moderate  $\Delta G^\ddagger$  and exergonic  $\Delta G_{\text{des}}$  allow both the electroreduction and desorption of \*NH<sub>2</sub>OH to occur at room temperature, in agreement with the formation of oxime and NH<sub>3</sub> as major products (Figures 4b).

## CONCLUSIONS

In conclusion, we have prepared a Zn<sub>93</sub>Cu<sub>7</sub> alloy that can drive the one-pot electrocatalysis of cyclohexanone oxime through

NO<sub>3</sub>R with a yield of 97% and FE of 27% at 100 mA/cm<sup>2</sup>. This electrochemical method not only enables the production of this important chemical precursor under mild conditions (room temperature, atmospheric pressure, aqueous solution, neutral pH, no toxic/expensive catalysts) compared to conventional chemical routes but also offers a promising strategy to upgrade nitrate into value-added organonitrogen compounds. In addition, this work demonstrates the central role of the \*NH<sub>2</sub>OH intermediate in this tandem EChem–Chem process, as well as the importance of controlling the surface adsorption of nitrogen species in electrosynthesis. The distinct behaviors of Zn, Cu, and ZnCu alloys observed in the experimental and theoretical studies reported in this work reveal that Cu-rich electrocatalysts can drive the NO<sub>3</sub>R at lower overpotentials to due to their strong affinity for NO<sub>3</sub><sup>−</sup> but favor further electroreduction of \*NH<sub>2</sub>OH into NH<sub>3</sub>. In contrast, Zn-rich electrocatalysts require higher overpotentials for NO<sub>3</sub>R but facilitate the chemical reaction between \*NH<sub>2</sub>OH and cyclohexanone to produce oxime. Overall, this work demonstrates a novel electrochemical strategy to upgrade nitrate and drive the sustainable synthesis of cyclohexanone oxime. This study also highlights the potential and key aspects for the development of EChem–Chem tandem processes for the electrification of industrial syntheses.

## ASSOCIATED CONTENT

### Supporting Information

The Supporting Information is available free of charge at <https://pubs.acs.org/doi/10.1021/acscatal.3c05388>.

Experimental and computational methods, compositions of different Zn/Cu catalysts, computed  $\Delta G_{nX}$  values, H-cell setup, chronopotentiometry graph, mass spec, NMR, HPLC and IC analysis of the products, SEM, EDX, ICP, ECSA, XRD, and XPS characterizations of the catalysts, reusability of the electrocatalyst, detection of NH<sub>2</sub>OH, nitrate reduction without cyclohexanone, and computational details for the surface coverage of electrocatalysts (PDF)

## AUTHOR INFORMATION

### Corresponding Authors

**Max García-Melchor** – School of Chemistry, CRANN and AMBER Research Centres, Trinity College Dublin, Dublin 2, Ireland; [orcid.org/0000-0003-1348-4692](https://orcid.org/0000-0003-1348-4692); Email: [garciamm@tcd.ie](mailto:garciamm@tcd.ie)

**Tengfei Li** – School of Chemistry and Environment, Manchester Metropolitan University, Manchester M1 5GD, United Kingdom; [orcid.org/0000-0002-8378-7130](https://orcid.org/0000-0002-8378-7130); Email: [t.li@mmu.ac.uk](mailto:t.li@mmu.ac.uk)

### Authors

**Jonathan Sharp** – School of Chemistry and Environment, Manchester Metropolitan University, Manchester M1 5GD, United Kingdom

**Anna Ciotti** – School of Chemistry, CRANN and AMBER Research Centres, Trinity College Dublin, Dublin 2, Ireland

**Hayley Andrews** – School of Chemistry and Environment, Manchester Metropolitan University, Manchester M1 5GD, United Kingdom

**Shaktiswaran R. Udayasurian** – School of Chemistry and Environment, Manchester Metropolitan University, Manchester M1 5GD, United Kingdom

Complete contact information is available at:  
<https://pubs.acs.org/10.1021/acscatal.3c05388>

## Author Contributions

<sup>§</sup>J.S. and A.C. have equal contributions to this work.

## Author Contributions

J.S. and T.L. performed the electrocatalysis experiments. T.L. designed and supervised the experimental studies. A.C. performed the DFT calculations. M.G.-M. designed and supervised the computational studies. H.A. performed the SEM and EDX measurements. J.S. and H.A. performed *in situ* Raman experiments. S.R.U., A.C., T.L., and M.G.-M. cowrote the first draft. All authors contributed to the final version of the manuscript.

## Notes

The authors declare no competing financial interest.

## ACKNOWLEDGMENTS

We appreciate the financial support by the RSC Research Fund (R21-3641011632), Science Foundation Ireland Research Centre Award (12/RC/2278\_P2), and Manchester Metropolitan University Research Accelerator Grant. We thank Dr. Gary Miller, Dr. David McKendry, and Dr. Claudio Dos Santos for instrument support.

## REFERENCES

- (1) *Global Nylon 6 Production Capacity reach to 8.86 million Tons in 2024*. HDIN Research, 2019.
- (2) Dahlhoff, G.; Niederer, J. P. M.; Hoelderich, W. F. *ε*-Caprolactam: new by-product free synthesis routes. *Catalysis Reviews* **2001**, *43* (4), 381–441.
- (3) Tauszik, G. R.; Crocetta, P. Production of hydroxylamine from nitrogen oxide: A short review. *Appl. Catal.* **1985**, *17* (1), 1–21.
- (4) Lewis, R. J.; Ueura, K.; Liu, X.; Fukuta, Y.; Davies, T. E.; Morgan, D. J.; Chen, L.; Qi, J.; Singleton, J.; Edwards, J. K.; Freakley, S. J.; Kiely, C. J.; Yamamoto, Y.; Hutchings, G. J. Highly efficient catalytic production of oximes from ketones using *in situ*-generated H<sub>2</sub>O<sub>2</sub>. *Science* **2022**, *376* (6593), 615–620.
- (5) Lewis, R. J.; Ueura, K.; Liu, X.; Fukuta, Y.; Qin, T.; Davies, T. E.; Morgan, D. J.; Stenner, A.; Singleton, J.; Edwards, J. K.; Freakley, S. J.; Kiely, C. J.; Chen, L.; Yamamoto, Y.; Hutchings, G. J. Selective Ammoxidation of Ketones via *In Situ* H<sub>2</sub>O<sub>2</sub> Synthesis. *ACS Catal.* **2023**, *13* (3), 1934–1945.
- (6) Thangaraj, A.; Sivasanker, S.; Ratnasamy, P. Catalytic properties of crystalline titanium silicalites III. Ammoxidation of cyclohexanone. *J. Catal.* **1991**, *131* (2), 394–400.
- (7) Cisneros, L. O.; Rogers, W. J.; Sam Mannan, M. Comparison of the thermal decomposition behavior for members of the hydroxylamine family. *Thermochim. Acta* **2004**, *414* (2), 177–183.
- (8) Mokaya, R.; Poliakov, M. A cleaner way to nylon? *Nature* **2005**, *437* (7063), 1243–1244.
- (9) Roffia, P.; Leofanti, G.; Cesana, A.; Mantegazza, M.; Padovan, M.; Petrini, G.; Tonti, S.; Gervasutti, P. Cyclohexanone Ammoxidation: A Break Through In The 6-Caprolactam Production Process. *Stud. Surf. Sci. Catal.* **1990**, *55*, 43–52.
- (10) Yan, M.; Kawamata, Y.; Baran, P. S. Synthetic Organic Electrochemical Methods Since 2000: On the Verge of a Renaissance. *Chem. Rev.* **2017**, *117* (21), 13230–13319.
- (11) Cha, H. G.; Choi, K. S. Combined biomass valorization and hydrogen production in a photoelectrochemical cell. *Nat. Chem.* **2015**, *7* (4), 328–333.
- (12) Li, T.; Kasahara, T.; He, J. F.; Dettelbach, K. E.; Sammis, G. M.; Berlinguette, C. P. Photoelectrochemical oxidation of organic substrates in organic media. *Nat. Commun.* **2017**, *8*, 390.
- (13) Jouny, M.; Lv, J.-J.; Cheng, T.; Ko, B. H.; Zhu, J.-J.; Goddard, W. A.; Jiao, F. Formation of carbon–nitrogen bonds in carbon monoxide electrolysis. *Nat. Chem.* **2019**, *11* (9), 846–851.
- (14) Han, G.; Li, G.; Sun, Y. Electrocatalytic dual hydrogenation of organic substrates with a Faradaic efficiency approaching 200%. *Nat. Catal.* **2023**, *6* (3), 224–233.
- (15) Chen, F. Y.; Wu, Z. Y.; Gupta, S.; Rivera, D. J.; Lamberts, S. V.; Pecaut, S.; Kim, J. Y. T.; Zhu, P.; Finfrook, Y. Z.; Meira, D. M.; King, G.; Gao, G.; Xu, W.; Cullen, D. A.; Zhou, H.; Han, Y.; Perea, D. E.; Muhich, C. L.; Wang, H. Efficient conversion of low-concentration nitrate sources into ammonia on a Ru-dispersed Cu nanowire electrocatalyst. *Nat. Nanotechnol.* **2022**, *17* (7), 759–767.
- (16) Fan, K.; Xie, W.; Li, J.; Sun, Y.; Xu, P.; Tang, Y.; Li, Z.; Shao, M. Active hydrogen boosts electrochemical nitrate reduction to ammonia. *Nat. Commun.* **2022**, *13* (1), 7958.
- (17) Liu, H.; Lang, X.; Zhu, C.; Timoshenko, J.; Rüscher, M.; Bai, L.; Guijarro, N.; Yin, H.; Peng, Y.; Li, J.; Liu, Z.; Wang, W.; Cuenya, B. R.; Luo, J. Efficient Electrochemical Nitrate Reduction to Ammonia with Copper-Supported Rhodium Cluster and Single-Atom Catalysts. *Angew. Chem., Int. Ed.* **2022**, *61* (23), No. e202202556.
- (18) Yang, J.; Qi, H.; Li, A.; Liu, X.; Yang, X.; Zhang, S.; Zhao, Q.; Jiang, Q.; Su, Y.; Zhang, L.; Li, J.-F.; Tian, Z.-Q.; Liu, W.; Wang, A.; Zhang, T. Potential-Driven Restructuring of Cu Single Atoms to Nanoparticles for Boosting the Electrochemical Reduction of Nitrate to Ammonia. *J. Am. Chem. Soc.* **2022**, *144* (27), 12062–12071.
- (19) Han, S.; Li, H.; Li, T.; Chen, F.; Yang, R.; Yu, Y.; Zhang, B. Ultralow overpotential nitrate reduction to ammonia via a three-step relay mechanism. *Nat. Catal.* **2023**, *6*, 402–414.
- (20) Wang, Y.; Xu, A.; Wang, Z.; Huang, L.; Li, J.; Li, F.; Wicks, J.; Luo, M.; Nam, D.-H.; Tan, C.-S.; Ding, Y.; Wu, J.; Lum, Y.; Dinh, C.-T.; Sinton, D.; Zheng, G.; Sargent, E. H. Enhanced Nitrate-to-Ammonia Activity on Copper–Nickel Alloys via Tuning of Intermediate Adsorption. *J. Am. Chem. Soc.* **2020**, *142* (12), 5702–5708.
- (21) Xu, H.; Ma, Y.; Chen, J.; Zhang, W.-x.; Yang, J. Electrocatalytic reduction of nitrate – a step towards a sustainable nitrogen cycle. *Chem. Soc. Rev.* **2022**, *51* (7), 2710–2758.
- (22) Chen, W.; Yang, X.; Chen, Z.; Ou, Z.; Hu, J.; Xu, Y.; Li, Y.; Ren, X.; Ye, S.; Qiu, J.; Liu, J.; Zhang, Q. Emerging Applications, Developments, Prospects, and Challenges of Electrochemical Nitrate-to-Ammonia Conversion. *Adv. Funct. Mater.* **2023**, *33*, 2300512.
- (23) van Langevelde, P. H.; Katsounaros, I.; Koper, M. T. M. Electrocatalytic Nitrate Reduction for Sustainable Ammonia Production. *Joule* **2021**, *5* (2), 290–294.
- (24) Li, J.; Zhang, Y.; Kuruvinashetti, K.; Kornienko, N. Construction of C–N bonds from small-molecule precursors through heterogeneous electrocatalysis. *Nat. Rev. Chem.* **2022**, *6* (5), 303–319.
- (25) Huang, Y.; Wang, Y.; Wu, Y.; Yu, Y.; Zhang, B. Electrocatalytic construction of the C–N bond from the derivatives of CO<sub>2</sub> and N<sub>2</sub>. *Science China Chemistry* **2022**, *65* (2), 204–206.
- (26) Lv, C.; Zhong, L.; Liu, H.; Fang, Z.; Yan, C.; Chen, M.; Kong, Y.; Lee, C.; Liu, D.; Li, S.; Liu, J.; Song, L.; Chen, G.; Yan, Q.; Yu, G. Selective electrocatalytic synthesis of urea with nitrate and carbon dioxide. *Nat. Sustain.* **2021**, *4* (10), 868–876.
- (27) Shin, S.; Sultan, S.; Chen, Z.-X.; Lee, H.; Choi, H.; Wi, T.-U.; Park, C.; Kim, T.; Lee, C.; Jeong, J.; Shin, H.; Kim, T.-H.; Ju, H.; Yoon, H. C.; Song, H.-K.; Lee, H.-W.; Cheng, M.-J.; Kwon, Y. Copper with an atomic-scale spacing for efficient electrocatalytic co-reduction of carbon dioxide and nitrate to urea. *Energy Environ. Sci.* **2023**, *16*, 2003–2013.
- (28) Wu, Y.; Jiang, Z.; Lin, Z.; Liang, Y.; Wang, H. Direct electrosynthesis of methylamine from carbon dioxide and nitrate. *Nat. Sustain.* **2021**, *4* (8), 725–730.
- (29) Kim, J. E.; Jang, J. H.; Lee, K. M.; Balamurugan, M.; Jo, Y. I.; Lee, M. Y.; Choi, S.; Im, S. W.; Nam, K. T. Electrochemical Synthesis of Glycine from Oxalic Acid and Nitrate. *Angew. Chem., Int. Ed.* **2021**, *60* (40), 21943–21951.

- (30) Luo, Y.; Xie, K.; Ou, P.; Lavallais, C.; Peng, T.; Chen, Z.; Zhang, Z.; Wang, N.; Li, X.-Y.; Grigioni, I.; Liu, B.; Sinton, D.; Dunn, J. B.; Sargent, E. H. Selective electrochemical synthesis of urea from nitrate and CO<sub>2</sub> via relay catalysis on hybrid catalysts. *Nat. Catal.* **2023**, *6*, 939.
- (31) Lan, J.; Wei, Z.; Lu, Y.-R.; Chen, D.; Zhao, S.; Chan, T.-S.; Tan, Y. Efficient electrosynthesis of formamide from carbon monoxide and nitrite on a Ru-dispersed Cu nanocluster catalyst. *Nat. Commun.* **2023**, *14* (1), 2870.
- (32) Guo, C.; Zhou, W.; Lan, X.; Wang, Y.; Li, T.; Han, S.; Yu, Y.; Zhang, B. Electrochemical Upgrading of Formic Acid to Formamide via Coupling Nitrite Co-Reduction. *J. Am. Chem. Soc.* **2022**, *144* (35), 16006–16011.
- (33) Wu, J.; Xu, L.; Kong, Z.; Gu, K.; Lu, Y.; Wu, X.; Zou, Y.; Wang, S. Integrated Tandem Electrochemical-chemical-electrochemical Coupling of Biomass and Nitrate to Sustainable Alanine. *Angew. Chem., Int. Ed.* **2023**, *62*, No. e202311196.
- (34) Li, M.; Wu, Y.; Zhao, B.-H.; Cheng, C.; Zhao, J.; Liu, C.; Zhang, B. Electrosynthesis of amino acids from NO and  $\alpha$ -keto acids using two decoupled flow reactors. *Nat. Catal.* **2023**, *6*, 906.
- (35) Zhang, X.; Jing, H.; Chen, S.; Liu, B.; Yu, L.; Xiao, J.; Deng, D. Direct electro-synthesis of valuable C = N compound from NO. *Chem. Catalysis* **2022**, *2* (7), 1807–1818.
- (36) Wu, Y.; Zhao, J.; Wang, C.; Li, T.; Zhao, B.-H.; Song, Z.; Liu, C.; Zhang, B. Electrosynthesis of a nylon-6 precursor from cyclohexanone and nitrite under ambient conditions. *Nat. Commun.* **2023**, *14* (1), 3057.
- (37) Wu, Y.; Chen, W.; Jiang, Y.; Xu, Y.; Zhou, B.; Xu, L.; Xie, C.; Yang, M.; Qiu, M.; Wang, D.; Liu, Q.; Liu, Q.; Wang, S.; Zou, Y. Electrocatalytic synthesis of nylon-6 precursor at almost 100% yield. *Angew. Chem., Int. Ed.* **2023**, *62*, No. e202305491.
- (38) Xiang, R.; Wang, S.; Liao, P.; Xie, F.; Kang, J.; Li, S.; Xian, J.; Guo, L.; Li, G. Electrocatalytic Synthesis of Pyridine Oximes using in Situ Generated NH<sub>2</sub>OH from NO species on Nanofiber Membranes Derived from NH<sub>2</sub>-MIL-53(Al). *Angew. Chem., Int. Ed.* **2023**, *62*, No. e202312239.
- (39) Kim, D. H.; Ringe, S.; Kim, H.; Kim, S.; Kim, B.; Bae, G.; Oh, H.-S.; Jaouen, F.; Kim, W.; Kim, H.; Choi, C. H. Selective electrochemical reduction of nitric oxide to hydroxylamine by atomically dispersed iron catalyst. *Nat. Commun.* **2021**, *12* (1), 1856.
- (40) Zhou, J.; Han, S.; Yang, R.; Li, T.; Li, W.; Wang, Y.; Yu, Y.; Zhang, B. Linear Adsorption Enables NO Selective Electroreduction to Hydroxylamine on Single Co Sites. *Angew. Chem., Int. Ed.* **2023**, *62* (27), No. e202305184.
- (41) Plowman, B. J.; Jones, L. A.; Bhargava, S. K. Building with bubbles: the formation of high surface area honeycomb-like films via hydrogen bubble templated electrodeposition. *Chem. Commun.* **2015**, *51* (21), 4331–4346.
- (42) Rahaman, M.; Kiran, K.; Zelocualtecatl Montiel, I.; Dutta, A.; Broekmann, P. Suppression of the Hydrogen Evolution Reaction Is the Key: Selective Electrosynthesis of Formate from CO<sub>2</sub> over Porous In<sub>35</sub>Cu<sub>45</sub> Catalysts. *ACS Appl. Mater. Interfaces* **2021**, *13* (30), 35677–35688.
- (43) Moreno-García, P.; Schlegel, N.; Zanetti, A.; Cedeño López, A.; Gálvez-Vázquez, M. d. J.; Dutta, A.; Rahaman, M.; Broekmann, P. Selective Electrochemical Reduction of CO<sub>2</sub> to CO on Zn-Based Foams Produced by Cu<sup>2+</sup> and Template-Assisted Electrodeposition. *ACS Appl. Mater. Interfaces* **2018**, *10* (37), 31355–31365.
- (44) Li, P.; Li, R.; Liu, Y.; Xie, M.; Jin, Z.; Yu, G. Pulsed Nitrate-to-Ammonia Electroreduction Facilitated by Tandem Catalysis of Nitrite Intermediates. *J. Am. Chem. Soc.* **2023**, *145* (11), 6471–6479.
- (45) Li, M.; Feng, C.; Zhang, Z.; Lei, X.; Chen, R.; Yang, Y.; Sugiura, N. Simultaneous reduction of nitrate and oxidation of by-products using electrochemical method. *J. Hazard. Mater.* **2009**, *171* (1), 724–730.
- (46) Dortsiou, M.; Katsounaros, I.; Polatides, C.; Kyriacou, G. Influence of the electrode and the pH on the rate and the product distribution of the electrochemical removal of nitrate. *Environ. Technol.* **2013**, *34* (3), 373–381.
- (47) Mácová, Z.; Bouzek, K. Electrocatalytic activity of copper alloys for NO<sub>3</sub><sup>-</sup> reduction in a weakly alkaline solution Part 1: Copper–zinc. *J. Appl. Electrochem.* **2005**, *35* (12), 1203–1211.
- (48) Wu, L.; Feng, J.; Zhang, L.; Jia, S.; Song, X.; Zhu, Q.; Kang, X.; Xing, X.; Sun, X.; Han, B. Boosting Electrocatalytic Nitrate-to-Ammonia via Tuning of N-Intermediate Adsorption on a Zn–Cu Catalyst. *Angew. Chem., Int. Ed.* **2023**, *62*, No. e202307952.
- (49) Gao, W.; Xie, K.; Xie, J.; Wang, X.; Zhang, H.; Chen, S.; Wang, H.; Li, Z.; Li, C. Alloying of Cu with Ru Enabling the Relay Catalysis for Reduction of Nitrate to Ammonia. *Adv. Mater.* **2023**, *35* (19), 2202952.
- (50) Butcher, D. P.; Gewirth, A. A. Nitrate reduction pathways on Cu single crystal surfaces: Effect of oxide and Cl<sup>-</sup>. *Nano Energy* **2016**, *29*, 457–465.
- (51) Sadergaski, L. R. Design of Experiments, Chemometrics, and Raman Spectroscopy for the Quantification of Hydroxylammonium, Nitrate, and Nitric Acid. *ACS Omega* **2022**, *7* (8), 7287–7296.
- (52) Hu, T.; Wang, C.; Wang, M.; Li, C. M.; Guo, C. Theoretical Insights into Superior Nitrate Reduction to Ammonia Performance of Copper Catalysts. *ACS Catal.* **2021**, *11* (23), 14417–14427.
- (53) Liu, J.-X.; Richards, D.; Singh, N.; Goldsmith, B. R. Activity and Selectivity Trends in Electrocatalytic Nitrate Reduction on Transition Metals. *ACS Catal.* **2019**, *9* (8), 7052–7064.
- (54) Wu, Y.; Lu, K.-K.; Xu, L.-H. Progress and prospects of electrochemical reduction of nitrate to restore the nitrogen cycle. *Journal of Materials Chemistry A* **2023**, *11* (33), 17392–17417.
- (55) Ciotti, A.; García-Melchor, M. The importance of surface coverages in the rational design of electrocatalysts. *Curr. Opin. Electrochem.* **2023**, *42*, No. 101402.
- (56) Li, T.; Ciotti, A.; Rahaman, M.; Yeung, C. W. S.; García-Melchor, M.; Reisner, E. Driving electrochemical organic hydrogenation on metal catalysts by tailoring hydrogen surface coverages. *ChemRxiv* **2023**.
- (57) Inta, H. R.; Dhanabal, D.; Markandaraj, S. S.; Shanmugam, S. Recent advances in electrocatalytic NO<sub>x</sub> reduction into ammonia. *EES Catalysis* **2023**, *1* (5), 645–664.
- (58) Soler-Jofra, A.; Pérez, J.; van Loosdrecht, M. C. M. Hydroxylamine and the nitrogen cycle: A review. *Water Res.* **2021**, *190*, No. 116723.